A New Finsler Minimal Path Model with Curvature Penalization for Image Segmentation and Closed Contour Detection

Da Chen and Laurent D. Cohen
CEREMADE, CNRS, University Paris Dauphine
PSL Research University, UMR 7534, 75016 PARIS, FRANCE
{chenda, cohen}@ceremade.dauphine.fr

Jean-Marie Mirebeau
Laboratoire de mathématiques d'Orsay, CNRS
Université Paris-Sud, Université Paris-Saclay, 91405 ORSAY, FRANCE
jean-marie.mirebeau@math.u-psud.fr

Abstract

In this paper, we propose a new curvature penalized minimal path model for image segmentation via closed contour detection based on the weighted Euler elastica curves, firstly introduced to the field of computer vision in [22]. Our image segmentation method extracts a collection of curvature penalized minimal geodesics, concatenated to form a closed contour, by connecting a set of user-specified points. Globally optimal minimal paths can be computed by solving an Eikonal equation. This first order PDE is traditionally regarded as unable to penalize curvature, which is related to the path acceleration in active contour models. We introduce here a new approach that enables finding a global minimum of the geodesic energy including a curvature term. We achieve this through the use of a novel Finsler metric adding to the image domain the orientation as an extra space dimension. This metric is non-Riemannian and asymmetric, defined on an orientation lifted space, incorporating the curvature penalty in the geodesic energy. Experiments show that the proposed Finsler minimal paths model indeed outperforms the-state-of-art minimal path models in both synthetic and real images.

1. Introduction

Active contours models have been considerably studied and used for object segmentation and feature extraction during almost three decades, since the pioneering work of the snakes model proposed by Kass *et al.* [15]. This approach models contours as closed curves locally minimizing an objective functional consisting of an internal and an external force. The internal force terms depend on the first and second order derivatives of the curves (snakes), and respectively account for a prior of small length and of low curvature of the contours. The external force is derived from a Potential, depending on image data such as gradient magnitudes [15], and designed to attracting the curves or snakes to image features of interest such as object boundaries.

The drawbacks of the snakes model [15] are its sensitivity to initialization, the difficulty of handling topological changes, and of minimizing the strongly non-convex path energy [13]. Regarding initialization, the snakes model requires an initial guess close to the desired images features, and preferably enclosing them because energy minimization tends to shorten the snakes. The introduction of an expanding balloon force allows the initial curve to be inside the objective region [11]. The issue of topology changes led, on the other hand, to the development of active contour methods which represent object boundaries as the zero level set of the solution to a PDE [9, 10, 17, 23, 30].

The difficulty of minimizing the non-convex snakes energy [15] leads to important practical problems, since the curve optimization procedure is often stuck at local minima of the energy functional, making the results sensitive to curve initialization and image noise. In order to find the global minimum of the active contours energy, Cohen and Kimmel proposed a geodesic or minimal path model [13] by removing the penalty associated to the second derivative of the curve from the snakes energy [15]. In contrast with snakes energy, this first order geodesic model [13] does not penalize curvature, despite its relevance for the applications. Thanks to this simplification, a fast, reliable and globally optimal numerical method allows to find the energy minimizing curve with prescribed endpoints; namely the fast marching method [27], based on the formalism of viscosity solutions to Eikonal PDE. These mathematical and algorithmic guarantees have important practical consequences, which allowed to deeply apply the minimal path model and its extensions to image analysis and medical imaging. In the Cohen-Kimmel model [13] tubular structures or object boundaries are extracted under the form of minimal paths with respect to an *isotropic* Riemannian metric over the image domain [3]. In [6, 8, 14], the *isotropic* metrics are replaced with more general *anisotropic* Riemannian metrics taking into account the orientation of the curves.

The above mentioned Eikonal PDE based minimal path models only consider the first derivative of the curve, failing to use the high order properties such as curvature to preserve the rigidity of the curves. Bekkers *et al.* [4,5] consider an orientation lifted sub-Riemannian geodesic model, first introduced by Petitot [25]. The numerical solver proposed in [4,5] is based on a PDE approach with upwind discretization scheme thus requiring expensive computational time. Additionally, minimal geodesics for Petitot's model occasionally feature *cusps*, which are annoying artifacts for the application of interest, and this kind of artifact does not appear in our approach. Reported computation times for this approach were initially completely impractical [4, 5], but one can obtain a hundred-fold reduction thanks to the use of state-of-the-art Fast Marching method [21].

Minimal paths based image segmentation methods [2, 3, 18, 19], as well as perceptual grouping methods [8, 12] represent boundaries as concatenations of geodesics. In [2], the authors took geodesics as active contours which can combine edge information for region-based active contours energy. In [18], the authors took a set of pre-computed minimal paths as candidate contours, and then find a combination minimizing the designed energy consisting of simplicity, edge and region information based terms. A combinatorial search then selects, among the admissible paths, an energy minimizing combination forming a closed contour. [2, 18] use the saddle points of the geodesic distance function to get a closed contour as the boundaries of an object. However, those models did not consider the curvature properties of the minimal paths.

Our contribution is twofold. Firstly, we propose a novel curvature penalized minimal path model for image segmentation through closed contour detection. We establish the connection between the Euler elastica, and minimal paths with respect to an orientation lifted asymmetric Finsler metric. We discuss options for geodesic distance and path computation, and settle for an adaptation of the Fast Marching method [21]. As a second contribution, we present a closed contour detection for image segmentation, in the form of piecewise *smooth* geodesics, connecting an user provided set of points distributed on an object boundary.

In Section 2 we briefly introduce the existing minimal path models, the concept of Finsler metric, and algorithms for distance computation and path extraction. The relationship between the Euler Elastica and the proposed Finsler metric is presented in Section 3 and the closed contour detection method is in Section 4.

2. Background and Motivation

2.1. General Minimal Path Model

The minimal path problem [26] is posed on a bounded domain Ω equipped with a metric $\mathcal{F}(x,\vec{u})$ depending on location $x\in\Omega$ and orientation $\vec{u}$. This application $\mathcal{F}$ defines at each point $x\in\Omega$ a norm $\mathcal{F}_x(\vec{u})=\mathcal{F}(x,\vec{u})$. These norms must be positive $\mathcal{F}_x(\vec{u})>0$ whenever $\vec{u}\neq 0$, 1-homogeneous, and obey the triangular inequality. However we allow them to be asymmetric: $\mathcal{F}_x(\vec{u})\neq\mathcal{F}_x(-\vec{u})$ in general. Let $\mathcal{A}_{p,x}$ be the set of all Lipschitz regular paths $\gamma:[0,\,1]\to\Omega$, *s.t.* $\gamma(0)=p$ and $\gamma(1)=x$, one measures path length through a metric $\mathcal{F}$:

$$\ell(\gamma)=\int_0^1\mathcal{F}_{\gamma(t)}\big(\gamma'(t)\big)\,dt, \tag{1}$$

where $\gamma'(t)=\frac{d}{dt}\gamma(t)$. The minimal action map $\mathcal{U}(x)$, or geodesic distance from the source point p, is the minimal length (1) among all path joining starting point p to $x\in\Omega$:

$$\mathcal{U}(x):=\min\{\ell(\gamma);\,\gamma\in\mathcal{A}_{p,x}\}. \tag{2}$$

The function $\mathcal{U}$ is the unique viscosity solution to an Eikonal PDE:

$$\begin{cases}\mathcal{F}_x^*\big(\nabla\mathcal{U}(x)\big)=1, & \text{for all } x\in\Omega,\\ \mathcal{U}(p)=0,\end{cases} \tag{3}$$

where the dual metric $\mathcal{F}^*$ is defined as

$$\mathcal{F}_x^*(\vec{u})=\sup_{\vec{v}\neq\mathbf{0}}\frac{\langle\vec{u},\vec{v}\rangle}{\mathcal{F}_x(\vec{v})}. \tag{4}$$

The metrics $\mathcal{F}$ considered in this paper combine a symmetric part, defined in terms of a positive tensor field $\mathcal{M}$, and an asymmetric part involving a vector field $\vec{\omega}$:

$$\mathcal{F}_x(\vec{u})=\sqrt{\langle\vec{u},\mathcal{M}(x)\,\vec{u}\rangle}-\langle\vec{\omega}(x),\vec{u}\rangle. \tag{5}$$

The asymmetric part should obey the following smallness condition to ensure that the Finsler metric is positive everywhere

$$s.t.\quad\langle\vec{\omega}(x),\mathcal{M}^{-1}(x)\vec{\omega}(x)\rangle<1. \tag{6}$$

The geodesic $\mathcal{C}$, joining $\mathbf{x}$ from $\mathbf{p}$, can be recovered by solving the following ODE involving $\mathcal{U}$ and the dual metric $\mathcal{F}^*$:

$$\mathcal{C}'(t)=-\nabla\mathcal{F}^*_{\mathcal{C}(t)}\Big(\nabla\mathcal{U}\big(\mathcal{C}(t)\big)\Big). \tag{7}$$

Equation (5) defines an anisotropic Finsler metric in general, an *anisotropic* Riemannian metric if the vector field $\vec{\omega}$ is identically zero, and an isotropic metric if in addition the tensor field $\mathcal{M}$ is everywhere diagonal.

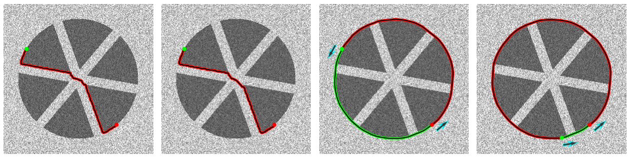
(a) (b) (c) (d)

Figure 1. Results from different minimal path models. (a) and (b) are the results from the Cohen-Kimmel model and the IL model respectively. (c) and (d) are the results from the proposed model.

2.2. Cohen-Kimmel Model and Orientation Lifting

The classical Cohen-Kimmel model in [13] is based on the energy functional:

$$\ell(\gamma) = \int_0^1 \left\{\epsilon + \mathcal{P}\big(\gamma(t)\big)\right\} \|\gamma'(t)\|\, dt. \tag{8}$$

Where $\mathcal{P}$ is the Potential function and $\epsilon > 0$ is a constant. The energy in (8) can be obtained from the more general formulation (1) and (5) by setting the tensor field $\mathcal{M}$ to be proportional to the identity matrix $\mathbf{I}_d$: $\mathcal{M}(x) = \big(\epsilon + \mathcal{P}(x)\big)^2 \mathbf{I}_d$, and setting $\vec{\omega} = \mathbf{0}$.

Orientation Lifted Metric Extension: The image domain Ω can be extended by product with an abstract parameter space [16]: $\bar{\Omega} = \Omega \times \mathbb{S}^1$, typically accounting for the orientation $\theta \in \mathbb{S}^1$ of the object boundary or tubular structure present in the processed image [24]. A lifted path $\gamma = (\Gamma, \theta)$ can be given the isotropic orientation-lifted Riemannian metric:

$$\mathcal{F}^{\mathrm{IL}}_{\gamma}(\gamma') = \frac{1}{\Phi_{\mathrm{IL}}(\Gamma, \theta)} \sqrt{\|\Gamma'\|^2 + \rho\, |\theta'|^2}, \tag{9}$$

corresponding to (5) with $\vec{\omega} = \mathbf{0}$. Φ_{IL} is a data driven velocity function. $\rho > 0$ is a constant. Orientation lifting often improves the results in [13], but suffers from the fact that nothing in (9) constrains the path direction Γ' to align with the orientation θ, a point which is addressed in our paper.

2.3. Computing the Action Map

In order to estimate the minimal action map $\mathcal{U}$, presented in (2) and (3), a discretization grid Z of the image domain Ω is introduced - or of the extended domain $\bar{\Omega}$ in the case of an orientation lifted metric. For each point $x \in \Omega$ or $\bar{\Omega}$, a small mesh $S(x)$ of a neighbourhood of x with vertices in Z is constructed. For example $S(x)$ is the square formed by the 4 neighbours of x in the classical Fast Marching on a regular orthogonal grid. In contrast with the Fast Marching method which solves the discrete approximation of the Eikonal PDE, an approximation of the minimal action map $\mathcal{U}$, with p as the initial source point, is calculated by solving the following fixed point system:

$$\begin{cases} \mathcal{U}(x) = \Lambda\mathcal{U}(x), & \text{for all } x \in Z, \\ \mathcal{U}(p) = 0, \end{cases} \tag{10}$$

where the involved Hopf-Lax update operator is defined by:

$$\Lambda\mathcal{U}(x) := \min_{y \in \partial S(x)} \left\{ \mathcal{F}_x(x - y) + \mathrm{I}_{S(x)}\, \mathcal{U}(y) \right\}, \tag{11}$$

where $\mathrm{I}_{S(x)}$ denotes the piecewise linear interpolation operator on the mesh $S(x)$, and y lies on the boundary of $S(x)$. The equality $\mathcal{U}(x) = \Lambda\mathcal{U}(x)$, replacing in (10) the Eikonal PDE: $\mathcal{F}^{\star}_x(\nabla\mathcal{U}(x)) = 1$ of (3), is a discretization of Bellman's optimality principle. It is similar in spirit to the Tsitsiklis approach [29]. It reflects the fact that the minimal geodesic $\mathcal{C}_{p,x}$, from p to x, has to cross the mesh boundary $\partial S(x)$ at least once at some point y; thus it is the concatenation of a geodesic $\mathcal{C}_{p,y}$ from p to y, which length is approximated by piecewise linear interpolation, and a very short geodesic $\mathcal{C}_{y,x}$ from y to x, approximated by a segment of curve length $\mathcal{F}_x(x - y)$.

The N-dimensional fixed point system (10), with $N = \#Z$, can be solved in a single pass using Fast Marching method [27], provided the stencils or mesh $S(x)$ at each point $x \in \Omega$ satisfies some geometric acuteness property depending on the local metric $\mathcal{F}_x$. An adaptive construction of such stencils S was introduced in [20] for anisotropic 3D Riemannian metric and in [21] for anisotropic 2D Finsler metric, which led to breakthrough improvements in terms of computation time and accuracy for strongly anisotropic geodesic energy metrics.

When the above mentioned geometric properties do not hold, the Fast Marching method is in principle not applicable, and slower multiple pass methods must be used instead such as the Adaptive Gauss Siedel Iteration (AGSI) of [7]. The present paper involves a 3D Finsler metric (14), for which we constructed stencils by adapting the 2D construction of [21]. Although these stencils lack the geometric acuteness condition, we found that the Fast Marching method still provided good approximations of the paths, while vastly improving computation times, see the next section. Future work will be devoted to improving the AGSI algorithm and/or our adaptive stencil construction for the Fast Marching algorithm to simultaneously benefit from a convergence guarantee and reasonable computation times.

2.4. Motivation

We show the geodesics for different given points from the Cohen-Kimmel model [13] in Fig. 1 (a), and isotropic orientation lifted model (IL) [24] in Fig. 1 (b). One can see that the mentioned two models suffer from the shortcuts problem because those models prefer to choose *shortest* paths, with respect to an image dependent metric promoting paths along image features. In contrast, the curvature penalty embedded in the proposed model favors *smooth* paths along image features as shown in Fig. 1 (c). As an additional benefit, the asymmetry of the proposed Finsler metric implies that the geodesic (red) from red dot to green dot is distinct from the one (green) from green dot to red dot: they correspond to complementary parts of the underlying object contour, see Fig. 1 (c) and (d).

3. Finsler Minimal Path Model

3.1. Euler Elastica

I add the parameter α in the formula The Euler elastica curves were first used in computer vision by Nitzberg and Mumford [22]. They minimize the following bending energy:

$$\mathcal{L}_0(\Gamma) = \int_0^L \big(1 + \alpha\kappa^2(s)\big)\, ds, \tag{12}$$

L is the classical curve length which is a free variable in our approach, s is the arc-length, and $\Gamma : [0, 1] \to \Omega$ is a regular curve with non-vanishing velocity. κ is the curvature of Γ.

The goal of this section is to cast the elastica bending energy (12) in the form of curve length with respect to a Finsler metric. Hence we transform the Elastica problem into finding a geodesic in a particular space. For this purpose, we denote by $\mathbb{S}^1 = [0,\, 2\pi)$ the angle space, with periodic boundary conditions, and let $\vec{v}_\theta = (\cos\theta, \sin\theta)$ be the unit vector corresponding to $\theta \in \mathbb{S}^1$.

Let $\Gamma(t) : [0, 1] \to \Omega$ be a smooth curve with non-vanishing velocity, and let $\gamma(t) = \big(\Gamma(t), \theta(t)\big)$ be its canonical orientation lifting, where $\theta(t)$ is defined such that $\vec{v}_{\theta(t)} = \Gamma'(t)/\|\Gamma'(t)\|$. Then it is well known that

$$\left(\frac{\Gamma'(t)}{\|\Gamma'(t)\|}\right)' = \kappa(t)\|\Gamma'(t)\| \left(\frac{\Gamma'(t)}{\|\Gamma'(t)\|}\right)^{\perp},$$

and

$$\begin{aligned}\left(\frac{\Gamma'(t)}{\|\Gamma'(t)\|}\right)' &= \frac{d}{dt}\vec{v}_{\theta(t)} \\ &= \theta'(t)\big(-\sin\theta(t), \cos\theta(t)\big) \\ &= \kappa(t)\|\Gamma'(t)\| \left(\frac{\Gamma'(t)}{\|\Gamma'(t)\|}\right)^{\perp},\end{aligned}$$

which yields to

$$\theta'(t) = \kappa(t)\|\Gamma'(t)\|.$$

Therefore, defining Euclidean arc-length by $ds = \|\Gamma'(t)\|dt$, one has

$$\begin{aligned}\int_0^L \big(1 + \alpha\kappa^2(s)\big)\, ds &= \int_0^1 \left(1 + \frac{\alpha|\theta'(t)|^2}{\|\Gamma'(t)\|^2}\right) \|\Gamma'(t)\|\, dt \\ &= \int_0^1 \mathcal{F}^{\infty}_{\gamma(t)}\big(\gamma'(t)\big)\, dt,\end{aligned}$$

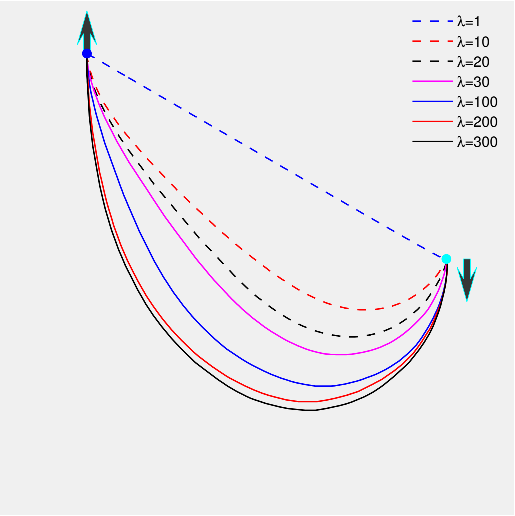

Figure 3. Approximated Euler elasticas for $\alpha = 500$ and different values of λ. Arrows indicate the initial and end tangents. Cyan and blue dots indicate the initial and end positions.

where we define the Finsler metric $\mathcal{F}^\infty$ as

$$\mathcal{F}^{\infty}_{\gamma}(\gamma') := \begin{cases} \|\Gamma'\| + \frac{\alpha\,|\theta'|^2}{\|\Gamma'\|}, & \text{if } \Gamma' \propto \vec{v}_\theta, \\ +\infty, & \text{otherwise.} \end{cases} \tag{13}$$

for any orientation lifted point $\gamma = (\Gamma, \theta) \in \Omega \times \mathbb{S}^1$, any vector $\gamma' = (\Gamma', \theta') \in \mathbb{R}^2 \times \mathbb{R}$ in the tangent space, and where $\propto$ denotes positive collinearity. Note that any other lifting $\tilde{\gamma}(t) = (\Gamma(t), \tilde{\theta}(t))$ of $\Gamma(t)$ would by construction of (13) have infinity energy.

3.2. λ-Penalized Anisotropic Finsler Metric $\mathcal{F}^\lambda$

The Finsler metric $\mathcal{F}^\infty$ defined in (13) is too singular to apply the Fast Marching algorithm directly. Hence we introduce a family of metrics which depend on a penalization parameter $\lambda \gg 1$ as follows:

$$\mathcal{F}^{\lambda}_{\gamma}(\gamma') := \sqrt{\lambda^2\|\Gamma'\|^2 + 2\alpha\lambda|\theta'|^2} - (\lambda - 1)\langle\vec{v}_\theta, \Gamma'\rangle, \tag{14}$$

for any $\gamma = (\Gamma, \theta) \in \Omega \times \mathbb{S}^1$ and any $\gamma' = (\Gamma', \theta') \in \mathbb{R}^2 \times \mathbb{R}$, and where $\vec{v}_\theta = (\cos\theta, \sin\theta)$.

A key object for visualizing and studying the geometry distortion induced by a metric is Tissot's indicatrix: the collection of unit balls in the tangent space. Here for $\gamma = (\Gamma, \theta) \in \Omega \times \mathbb{S}^1$ and $\lambda \in [1, \infty]$

$$B^{\lambda}_{\gamma} := \{\gamma' = (\Gamma', \theta') \in \mathbb{R}^2 \times \mathbb{R};\ \mathcal{F}^{\lambda}_{\gamma}(\gamma') \le 1\}. \tag{15}$$

Let $\Gamma'_{\|} := \langle\Gamma', \vec{v}_\theta\rangle$ and $\Gamma'_{\perp} = \langle\Gamma', \vec{v}_\theta^{\perp}\rangle$. Then $\gamma' = (\Gamma', \theta') \in B^{\infty}_{\gamma}$ is characterized by $\Gamma'_{\perp} = 0$, inequality $\Gamma'_{\|} > 0$ and

$$\Gamma'_{\|} + \frac{\alpha|\theta'|^2}{\Gamma'_{\|}} \le 1 \quad \Leftrightarrow \quad \left(\Gamma'_{\|} - \frac{1}{2}\right)^2 + \alpha|\theta'|^2 \le \frac{1}{4}.$$

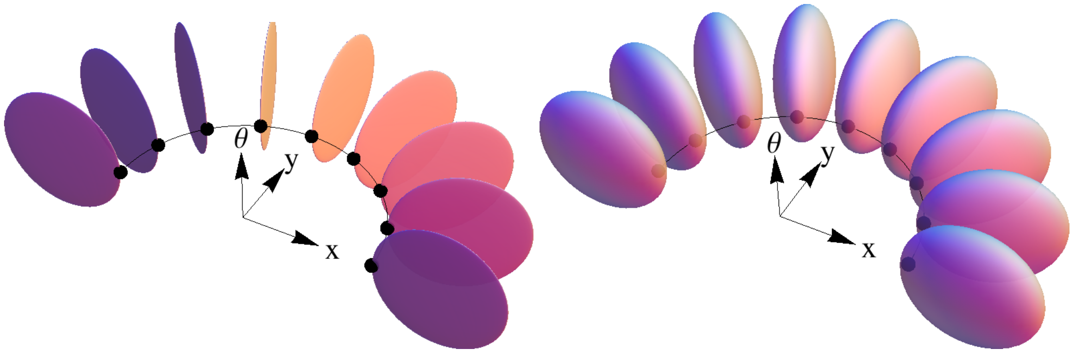

(a) (b)

Figure 2. Visualization for $\mathcal{F}^\infty$ and $\mathcal{F}^\lambda$ with $\alpha = 1$ by Tissot's indicatrix. (a): Tissot's indicatrix for the metric $\mathcal{F}^\infty$ with $\alpha = 1$ are flat 2D disks embedded in 3D space, aligned with the direction $\vec{v}_\theta$ (several directions θ shown). (b): Tissot's indicatrix for $\mathcal{F}^\lambda$ are ellipsoids, which are flatten and approximate a limit disk as $\lambda \to \infty$.

Thus B_γ^∞ is a flat 2D ellipse embedded in the 3D tangent space, and containing the origin on its boundary. Particularly, when $\alpha = 1$, B_γ^∞ turns to a flat 2D disk of radius $1/2$ as shown in Fig. 2 (a). On the other hand when $\lambda < \infty$, a short computation shows that B_γ^λ is characterized by a quadratic equation

$$\frac{\lambda}{2}\Gamma_\perp'^2 + a_\lambda\left(\Gamma_\parallel' - \frac{b_\lambda}{2}\right)^2 + \alpha|\theta'|^2 \le \frac{c_\lambda}{4}, \qquad (16)$$

where $a_\lambda, b_\lambda, c_\lambda$ are all $1 + \mathcal{O}(1/\lambda)$. Hence B_γ^λ is an ellipsoid, for instance see Fig. 2 (b) with $\alpha = 1$, almost flat in the direction of $\vec{v}_\theta^\perp$ due to the large factor $\lambda/2$, which converges to the flat disk B_γ^∞ in the Haussdorf distance as $\lambda \to \infty$.

Tissot's indicatrix is also the *control set* in the optimal control interpretation of the Eikonal equation (3). The Haussdorf convergence of the control sets shows that the action map and minimal paths for the metric $\mathcal{F}^\lambda$ converge towards those of $\mathcal{F}^\infty$ as $\lambda \to \infty$. When λ is sufficiently large, the spatial and angular resolutions are sufficiently small, the fixed point system (10) is properly solved, and the minimal paths are properly extracted (7), one obtains numerical convergence of the extracted curves towards the Euler elasticas, as illustrated on Fig. 3.

The metric $\mathcal{F}^\lambda$ has precisely the required form (5) with tensor field $\mathcal{M} = \mathrm{diag}(\lambda^2, \lambda^2, 2\lambda)$ and vector field $\vec{\omega} = (\lambda - 1)(\vec{v}_\theta, 0) \in \mathbb{R}^2 \times \mathbb{R}$. Note that the definiteness constraint (6) is satisfied:

$$\langle \vec{\omega}, \mathcal{M}^{-1}\vec{\omega}\rangle = (1 - \lambda^{-1})^2 < 1.$$

The anisotropy ratio $\mu(\mathcal{F})$ characterizes the distortion between different orientations induced by a metric $\mathcal{F}$ on a domain $\bar{\Omega}$. Letting $\mathbf{x} \in \bar{\Omega}$, the anisotropic ratio $\mu(\mathcal{F}^\lambda)$ of the proposed Finsler metric $\mathcal{F}^\lambda$ (14) is defined by

$$\mu(\mathcal{F}^\lambda) := \sup_{\mathbf{x}\in\bar{\Omega}}\left\{\max_{|\vec{u}|=|\vec{v}|=1}\left\{\frac{\mathcal{F}_{\mathbf{x}}^\lambda(\vec{u})}{\mathcal{F}_{\mathbf{x}}^\lambda(\vec{v})}\right\}\right\}. \qquad (17)$$

Table 1. CPU time (in seconds) for $\alpha = 500$ and different values of λ with Fast Marching algorithm on a $300^2 \times 108$ grid.

λ	1	10	20	30	100	200	300
time	15.5	25.8	27.0	28.4	31.7	33.6	34.7

Table 2. Average number of Hopf-Lax updates required for each grid point by AGSI for different values of λ on a $120^2 \times 43$ grid.

λ:	1	4	6	64	256	1024
	3	36	67	90	259	349

As an example, for the Finsler metric $\mathcal{F}^\lambda$ (14), with $\lambda \ge 2$ and $\alpha = 1$, one maximizes (17) by choosing $\vec{u} = -\vec{v}_\theta$ and $\vec{v} = \vec{v}_\theta$, so that

$$\mu(\mathcal{F}^\lambda) = 2\lambda - 1.$$

Numerically, anisotropy is related to the problem *stiffness*, hence to its difficulty. We observe on Table 1 a logarithmic dependence of computational (CPU) time with respect to anisotropy on a synthetic image with size of $300^2 \times 108$ for $\alpha = 500$ and different values of λ. I would like to delete this sentence—[multiplying λ by 10 adds about 6 seconds of CPU time, with $N = 300^2 \times 108$ grid points.] These observations agree with the worst case analysis of method [21], which yields the upper bound $\mathcal{O}(N\ln^3\mu + N\ln N)$, depending poly-logarithmically on the anisotropy ratio μ (17) and quasi-linearly on the number N of discretization points in $\bar{\Omega}$. In contrast, methods such as [28] displaying a polynomial complexity $\mathcal{O}(N\mu^{d-1})$ in the anisotropy ratio would be unworkable. The iterative AGSI method, on the other hand, requires hundreds of operator (11) evaluations per grid point to converge for large anisotropies $\lambda \gg 1$, see Table 2, which also leads to prohibitive computation times, thus impractical.

In Fig. 3, we show different geodesics (approximated Euler elasticas) with different values of λ. The arrows indicate the initial and end directions. Cyan and blue dots indicate the initial position and end position respectively. In this experiment, we set the angle resolution to be $\theta_s = 2\pi/108$ and image size is 300×300. When $\lambda = 1$, the metric $\mathcal{F}^\lambda$ is constant over the domain, since the coefficient in front of $\vec{v}_\theta$ vanishes. Hence the minimal geodesics are straight lines, see Fig. 3, that do not align with the prescribed endpoints tangents. As λ increases, curvature penalization forces the extracted paths to gradually align with the prescribed endpoints tangents and take the elastic shape.

3.3. Weighted λ-Penalized Finsler Metric $\mathcal{J}$

In Section 3.2, we have introduced the anisotropic λ-Penalized Finsler metric $\mathcal{F}^\lambda$ to efficiently approximate the Euler elastica [22]. In order to apply this minimal path model to image analysis, like object segmentation, we incorporate the image data to the proposed Finsler metric $\mathcal{F}^\lambda$, defining a metric $\mathcal{J} : \Omega \times \mathbb{S}^1 \to \mathbb{R}^+$ by

$$\mathcal{J}_\gamma(\gamma') = \sqrt{\frac{\lambda^2\|\Gamma'\|^2}{\Phi_b^2} + \frac{2\lambda|\theta'|^2}{\Phi_b\beta_b^2}} - (\lambda-1)\frac{\langle\vec{v}_\theta, \Gamma'\rangle}{\Phi_b}, \quad (18)$$

where Φ_b and β_b are image data driven speed functions. The computation of Φ and β_b is described in Section 4.1.

The Finsler metric $\mathcal{J}$ is used to approximate the weighted Euler elastica energy:

$$\mathcal{L}(\gamma) = \int_0^L \left(\frac{1}{\Phi_b(\gamma(s))} + \frac{\kappa^2(s)}{\beta_b^2(\gamma(s))}\right) ds, \quad (19)$$

where s is the arc-length and L is the classical curve length. The minimal action map associated to metric $\mathcal{J}$ is denoted by $\mathcal{W}_\mathbf{p}$, and estimated through the fast marching algorithm as explained in Section 2.3.

4. Image Segmentation via Contour Detection

In this section, we introduce an image segmentation method based on the Finsler minimal path model proposed in Section 3.3.

4.1. Gradient Magnitude Based Φ_b and β_b

Consider a color image, which we regard as a vector valued map $\mathbf{I} : \Omega \to \mathbb{R}^3$, $\mathbf{I}(x) = [I_1(x), I_2(x), I_3(x)]$ for each $x \in \Omega$. Let $\mathbf{I}^\sigma := G^\sigma * \mathbf{I} = [I_1^\sigma, I_2^\sigma, I_3^\sigma]$, where G^σ is a Gaussian function of fixed variance σ. The gradient $\nabla\mathbf{I}^\sigma$ is a 2×3 Jacobian matrix of rows ∇I_k^σ, $1 \leq i \leq 3$.

For object boundaries extraction, we consider velocity functions Φ_b and β_b independent from the angle $\theta \in \mathbb{S}^1$, and determined by the image gradient:

$$\Phi_b(x, \cdot) = 1 + \eta\frac{\|\nabla\mathbf{I}^\sigma(x)\|_F}{\max\{\|\nabla\mathbf{I}^\sigma(z)\|_F; z \in \Omega\}}, \quad (20)$$

$$\beta_b(x, \cdot) = \sqrt{\Phi_b(x, \cdot)/\alpha_0}, \quad \text{or} \quad \beta_b = \text{constant}, \quad (21)$$

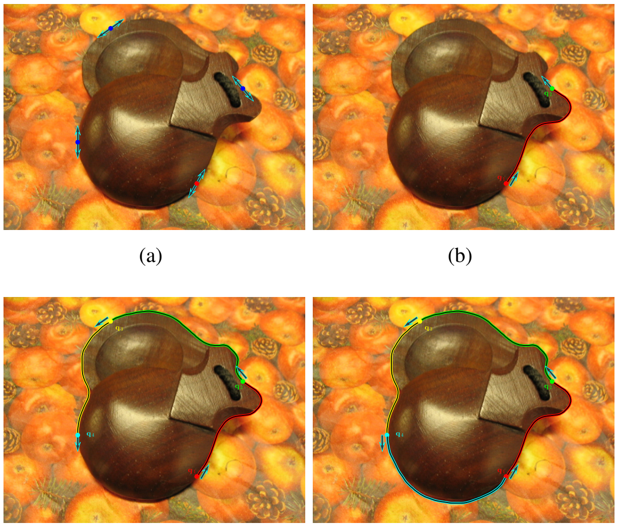
(a) (b)
(c) (d)

Figure 4. Steps of our contour detection algorithm (see text).

where α_0, η and σ are positive constants. $\|\cdot\|_F$ is the Frobenius norm: $\|\nabla\mathbf{I}^\sigma(x)\|_F = \sqrt{\sum_{k=1}^3 \|\nabla I_k^\sigma(x)\|^2}$, $\forall x \in \Omega$. We use a definition of Φ_b that do not depend on the orientation since in the examples of the next sections, we show that the curvature term is powerful enough to find the good contours with this simple image-dependant information.

4.2. Closed Contour Detection as A Set of Piecewise Smooth Finsler Minimal Paths.

Consider a collection of user-specified physical positions $\mathcal{H} := \{x_i \in \Omega, i = 1, 2, ..., m\}$ with $m \geq 2$, all of which are on the boundary of the object. The goal is to find a closed contour linking those physical points in $\mathcal{H}$ by curvature penalized geodesics to form a complete boundary of the object. We denote the orientation lifting of $\mathcal{H}$ by $\mathcal{D}$:

$$\mathcal{D} := \Big\{\mathbf{x}_i = (x_i, \theta_i), \, \widetilde{\mathbf{x}}_i = (x_i, \mathrm{mod}(\theta_i + \pi, 2\pi)), \\ i = 1, 2, ..., m, \, \theta_i \in [0, 2\pi)\Big\},$$

where the directions θ_i can be manually specified, or calculated using the rotated image gradient field. We show those vertices in Fig. 4 (a) by blue and red dots denoting the physical positions. The arrows indicate the corresponding tangents. Each point $x_i \in \mathcal{H}$ corresponds two orientation lifted vertices: $\mathbf{x}_i$ and $\widetilde{\mathbf{x}}_i$ in $\mathcal{D}$ with opposite tangents. **Notation**: if $\mathbf{p} = (p, \theta_p)$ is a vertex in $\mathcal{D}$, then we use $\widetilde{\mathbf{p}} = (p, \mathrm{mod}((\theta_p + \pi), 2\pi))$ to denote the vertex which has the same physical position with $\mathbf{p}$ but opposite tangents.

We start the proposed closed contour detection method by selecting the first physical position, assuming as x_1. Then the orientation lifted vertices of x_1 are denoted by

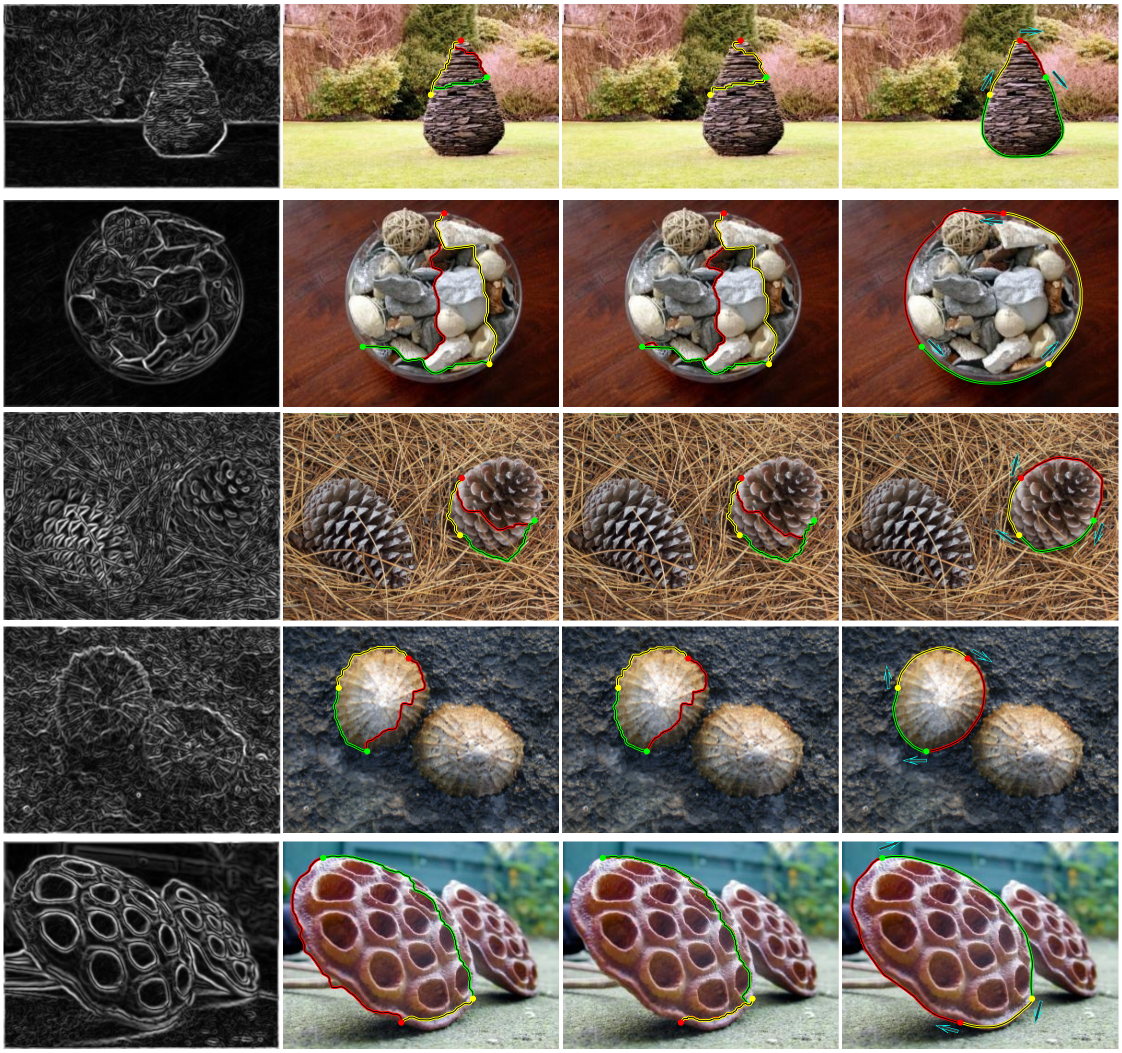

Figure 7. Contour detection results from different models. **Column 1** show the edge maps. **Columns 2-4** show the contour detection results from the Cohen-Kimmel model, the IL model and the proposed model.

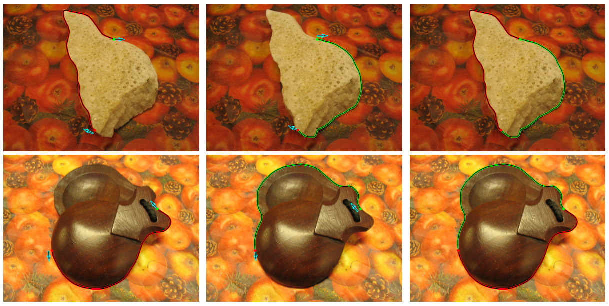

Figure 5. Geodesics from the proposed model. **Column 1**: red dots are initial source points. **Column 2**: green dots are initial source points. **Column 3**: closed contours combining the two geodesics.

$\mathbf{x}_1,\ \widetilde{\mathbf{x}}_1 \in \mathcal{D}$. Once x_1 is specified, we remove $\mathbf{x}_1$ and $\widetilde{\mathbf{x}}_1$ from $\mathcal{D}$. In Fig. 4 (a), we denote $\mathbf{x}_1, \widetilde{\mathbf{x}}_1$ by red dot with two arrows. Let $\mathbf{z}_1 \in \mathcal{D}$ be the closest vertex to $\mathbf{x}_1$ in terms of geodesic distance $\mathcal{W}_{\mathbf{x}_1}$ as discussed in Section 3.3, i.e., $\mathbf{z}_1 = \arg\min_{\mathbf{z}\in\mathcal{D}} \mathcal{W}_{\mathbf{x}_1}(\mathbf{z})$. Similarly to $\mathbf{z}_1$, we define the closest vertex $\mathbf{z}_2 \in \mathcal{D}$ of $\widetilde{\mathbf{x}}_1$. With those definitions, the first and second vertices $\mathbf{q}_1,\ \mathbf{q}_2$ are chosen simultaneously:

$$(\mathbf{q}_1, \mathbf{q}_2) = \begin{cases} (\mathbf{x}_1, \mathbf{z}_1), \text{ if } \mathcal{W}_{\mathbf{x}_1}(\mathbf{z}_1) < \mathcal{W}_{\widetilde{\mathbf{x}}_1}(\mathbf{z}_2), \\ (\widetilde{\mathbf{x}}_1, \mathbf{z}_2), \text{ otherwise.} \end{cases} \tag{22}$$

$\mathbf{q}_1$ and $\mathbf{q}_2$ are shown in Fig. 4 (b). If the action map $\mathcal{W}_{\mathbf{x}_1}$ (resp. $\mathcal{W}_{\widetilde{\mathbf{x}}_1}$) is computed via the Fast Marching algorithm, the vertex $\mathbf{z}_1$ (resp. $\mathbf{z}_2$) is the first one reached by the front, which is monotonically advancing. Once q_1, q_2 are found, the geodesic $\mathcal{C}_{\mathbf{q}_1,\mathbf{q}_2}$ can be recovered using (7) and $\mathbf{q}_2$, $\widetilde{\mathbf{q}}_2$ will be removed from $\mathcal{D}$. Taking $\mathbf{q}_2$ as the initial source point for Fast Marching algorithm, we find next vertex by

$$\mathbf{q}_3 = \arg\min_{\mathbf{z}\in\mathcal{D}} \mathcal{W}_{\mathbf{q}_2}(\mathbf{z}),$$

Figure 6. Results from different minimal path models. Columns 1-3 are the results from the Cohen-Kimmel model, the IL model and the proposed model respectively.

and remove $\mathbf{q}_3$, $\widetilde{\mathbf{q}}_3$ from $\mathcal{D}$. Then the geodesic $\mathcal{C}_{\mathbf{q}_2,\mathbf{q}_3}$ can be tracked. When the final point $\mathbf{q}_m$ is found, as an example see $\mathbf{q}_3$ in Fig. 4 (c), the geodesic $\mathcal{C}_{\mathbf{q}_m,\mathbf{q}_1}$ is computed by simply letting $\mathbf{q}_m$ be the initial source point and $\mathbf{q}_1$ be the endpoint as the curve labeled by cyan in Fig. 4 (d). This method simply matches points by pairs, joining a vertex to the remaining nearest neighbour w.r.t. the geodesic distance, so as to form a closed contour. Note importantly, that the obtained piecewise geodesic contour is **smooth** (C^1 differentiable) since the endpoint/startpoint of consecutive geodesics have both matching positions q_i and orientations θ_i. In summary, this detection method aims to seeking a set χ of pairs of points:

$$\chi = \bigcup_{i=1}^{m-1} \{(\mathbf{q}_i,\, \mathbf{q}_{i+1})\} \bigcup \{(\mathbf{q}_m,\, \mathbf{q}_1)\}, \tag{23}$$

and a set of Finsler minimal paths denoted by $\mathcal{C}$, joining all the pairs of points in χ.

The proposed detection procedure benefits from the asymmetry of the proposed Finsler minimal paths. In Fig. 5, we show this asymmetric property by exchanging the initial and end vertices. The extracted minimal paths in the left and right columns pass different parts of the boundaries of the objects. While for symmetric metric, exchanging initial and end vertices will lead to the same extracted geodesic. In the right column of Fig. 5, the closed contours are combined by the extracted geodesics, which means that, at least in some simple cases, extracting the full closed contour of an object only requires two vertices by the proposed contour detection without using the saddle points as in [18].

5. Experiments

In the following experiments, we suppose that a path has the same visualized colour as its initial point. For instance, the red dot corresponds to the initial point of a geodesic labeled by red. We set $\lambda = 100$ see (14), for all the following experiments and the resolution for orientation dimension is $2\pi/72$. To demonstrate the advantages of using curvature penalty and asymmetric Finsler metric, we compare the Cohen-Kimmel model [13], the IL model [24] and the proposed model. For the IL model we use the metric in (9) corresponding to $\Phi_{\mathrm{IL}}(\cdot,\theta_\pi) = \Phi_b(\cdot,\theta_\pi)$, $\theta_\pi \in [0,\,\pi)$ and $\rho = \alpha_0$, where α_0 is used in (21).

The intuitive application of the minimal path models is to extract geodesics for given initial source points and endpoints as shown in Fig. 6 tested on Weizmann data set [1]. In Fig. 6, columns 1-3 are the results from the Cohen-Kimmel model [13], the IL model [24] and the proposed model respectively, with red dots indicating the initial positions and green points as the end positions. One can see that our model can obtain the correct and smooth minimal paths thanks to the curvature penalty.

In Fig. 7, we show the contour detection results in nature images [1] from three models: Cohen-Kimmel model, the IL model and the proposed model in columns 2-4. In the first column we demonstrate the normalized Frobenius norm (not Φ_b). In this experiment, we first identify the collection χ in (23) by the proposed contour detection procedure described in Section 4. Then the contour detection results in second and third columns are obtained by simply using the geodesics recovered by the Cohen-Kimmel and the IL models to link all the pairs of points in the just-identified χ respectively. It can be seen that the results from the Cohen-Kimmel and the IL models suffer from *short cuts* due to the lack of curvature regularization while the results in the final column produced by the proposed model with suitable curvature penalty can avoid such *short cuts*. I removed the Fig. 8 as we have no space for those pictures. If possible, I could add the pictures in Fig.8 to Fig. 7 as the last column

6. Conclusion

In this paper, we consider a minimal path model with curvature penalty, the Mumford/Euler weighted elastica curves, implemented via orientation lifted Finsler metrics. We show that the extracted curvature penalized geodesics can be concatenated into a smooth closed contour for object segmentation. The proposed Finsler metric enforces the contour smoothness, and a strong asymmetry which benefits to the method. Comparing to the state-of-the-art minimal path models, our model could get much better contour detection results even for the objects with weak edges.

Acknowledgement

This work was partially supported by ANR grant NS-LBR, ANR-13-JS01-0003-01.

References

[1] S. Alpert, M. Galun, A. Brandt, and R. Basri. Image segmentation by probabilistic bottom-up aggregation and cue integration. *IEEE Transactions on Pattern Analysis and Machine Intelligence*, 34(2):315–327, 2012. 8

[2] V. Appia and A. Yezzi. Active geodesics: Region-based active contour segmentation with a global edge-based constraint. In *Proc. ICCV 2011*, pages 1975–1980, 2011. 2

[3] B. Appleton and H. Talbot. Globally optimal geodesic active contours. *Journal of Mathematical Imaging and Vision*, 23(1):67–86, 2005. 2

[4] E. Bekkers, R. Duits, A. Mashtakov, and G. Sanguinetti. Data-Driven Sub-Riemannian Geodesics in SE (2). In *Proc. SSVM 2015*, pages 613–625, 2015. 2

[5] E. J. Bekkers, R. Duits, A. Mashtakov, and G. R. Sanguinetti. A pde approach to data-driven sub-riemannian geodesics in se (2). *SIAM Journal on Imaging Sciences*, 8(4):2740–2770, 2015. 2

[6] F. Benmansour and L. Cohen. Tubular Structure Segmentation Based on Minimal Path Method and Anisotropic Enhancement. *International Journal of Computer Vision*, 92(2):192–210, 2011. 2

[7] F. Bornemann and C. Rasch. Finite-element Discretization of Static Hamilton-Jacobi Equations based on a Local Variational Principle. *Computing and Visualization in Science*, 9(2):57–69, 2006. 3

[8] S. Bougleux, G. Peyré, and L. Cohen. Anisotropic Geodesics for Perceptual Grouping and Domain Meshing. In *Proc. ECCV 2008*, pages 129–142, 2008. 2

[9] V. Caselles, F. Catté, T. Coll, and F. Dibos. A geometric model for active contours in image processing. *Numerische mathematik*, 66(1):1–31, 1993. 1

[10] V. Caselles, R. Kimmel, and G. Sapiro. Geodesic active contours. *International Journal of Computer Vision*, 22(1):61–79, 1997. 1

[11] L. Cohen. On active contour models and balloons. *CVGIP: Image understanding*, 53(2):211–218, 1991. 1

[12] L. Cohen. Multiple contour finding and perceptual grouping using minimal paths. *Journal of Mathematical Imaging and Vision*, 14(3):225–236, 2001. 2

[13] L. Cohen and R. Kimmel. Global minimum for active contour models: A minimal path approach. *International Journal of Computer Vision*, 24(1):57–78, 1997. 1, 2, 3, 8

[14] S. Jbabdi, P. Bellec, R. Toro, J. Daunizeau, M. Pélégrini-Issac, and H. Benali. Accurate anisotropic fast marching for diffusion-based geodesic tractography. *Journal of Biomedical Imaging*, 2008:2, 2008. 2

[15] M. Kass, A. Witkin, and D. Terzopoulos. Snakes: Active contour models. *International Journal of Computer Vision*, 1(4):321–331, 1988. 1

[16] R. Kimmel and J. Sethian. Optimal algorithm for shape from shading and path planning. *JJournal of Mathematical Imaging and Vision*, 14(3):237–244, 2001. 3

[17] R. Malladi, J. Sethian, and B. Vemuri. Evolutionary fronts for topology-independent shape modeling and recovery. In *Proc. ECCV'94*, pages 1–13, 1994. 1

[18] J. Mille, S. Bougleux, and L. Cohen. Combination of piecewise-geodesic paths for interactive segmentation. *International Journal of Computer Vision*, 112(1):1–22, 2014. 2, 8

[19] J. Mille and L. D. Cohen. Geodesically linked active contours: evolution strategy based on minimal paths. In *Proc. SSVM 2009*, pages 163–174. 2009. 2

[20] J.-M. Mirebeau. Anisotropic Fast-marching on Cartesian Grids Using Lattice Basis Reduction. *SIAM Journal on Numerical Analysis*, 52(4):1573–1599, 2014. 3

[21] J.-M. Mirebeau. Efficient fast marching with Finsler metrics. *Numerische mathematik*, 126(3):515–557, 2014. 2, 3, 5

[22] M. Nitzberg and D. Mumford. The 2.1-D sketch. In *Proc. ICCV 1990*, pages 138–144, 1990. 1, 4, 6

[23] S. Osher and J. Sethian. Fronts propagating with curvature-dependent speed: algorithms based on hamilton-jacobi formulations. *Journal of Computational Physics*, 79(1):12–49, 1988. 1

[24] M. Péchaud, R. Keriven, and G. Peyré. Extraction of tubular structures over an orientation domain. In *Proc. CVPR 2009*, pages 336–342, 2009. 3, 8

[25] J. Petitot. The neurogeometry of pinwheels as a sub-Riemannian contact structure. *Journal of Physiology-Paris*, 97(2-3):265–309, 2003. 2

[26] G. Peyré, M. Péchaud, R. Keriven, and L. D. Cohen. Geodesic Methods in Computer Vision and Graphics. *Foundations and Trends in Computer Graphics and Vision*, pages 197–397, 2010. 2

[27] J. Sethian. Fast marching methods. *SIAM Review*, 41(2):199–235, 1999. 1, 3

[28] J. Sethian and A. Vladimirsky. Ordered upwind methods for static Hamilton-Jacobi equations. *Proceedings of the National Academy of Sciences*, 98(20):11069–11074 (electronic), 2001. 5

[29] J. N. Tsitsiklis. Efficient algorithms for globally optimal trajectories. *IEEE Transactions on Automatic Control*, 40(9):1528–1538, 1995. 3

[30] A. Yezzi, S. Kichenassamy, A. Kumar, P. Olver, and A. Tannenbaum. A geometric snake model for segmentation of medical imagery. *IEEE Transaction on Medical Imaging*, 16(2):199–209, 1997. 1